

1 Revision 1

2 Word Count: 5035

3 **Molybdenum isotopic fractionation in the Panzihua mafic layered intrusion in**
4 **the Emeishan large igneous province, southwest China**

Le Zhang^{1,2*}, Jie Li^{1,2}, Yan Zhang³, Bing-Yu Peng^{1,2}, Zhi-Bing Wang^{1,2}, Zhong-Yuan
Ren^{1,2}

¹ State Key Laboratory of Isotope Geochemistry, Guangzhou Institute of
Geochemistry, Chinese Academy of Sciences, Guangzhou 510640, China.

9 ² CAS Center for Excellence in Deep Earth Science, Guangzhou 510640, China.

10 ³ Key Laboratory of Marine Geology and Metallogeny, First Institute of
11 Oceanography, Ministry of Natural Resources, Qingdao 266061, China

12

13

14

15

16

17 * Correspondence to:
18 zhangle@gig.ac.cn

19

Abstract The large Mo isotopic fractionations between different geological reservoirs make this isotopic system a potential useful tool for constraining the origins of magmatism. However, the effect of magmatic differentiation on Mo isotopes is still controversial. In this study, we obtained Mo isotope data for the Panzhihua gabbroic intrusion (i.e., including mineral separates of clinopyroxene, plagioclase, magnetite, and ilmenite). The whole-rock samples and mineral separates exhibit large Mo isotopic fractionations with $\delta^{98/95}\text{Mo}$ values as follows: magnetite (−0.73‰ to −0.32‰) < clinopyroxene (−0.32‰ to −0.10‰) < ilmenite (0.06‰ to 0.36‰) < plagioclase (0.33‰ to 0.83‰). Iron–Ti oxides have Mo contents that are one order of magnitude higher than those of clinopyroxene and plagioclase. Mass balance calculations based on Mo isotopes and contents are consistent with an adcumulate origin for the Panzhihua intrusion. Rayleigh fractionation modeling shows that removal of magnetite and ilmenite results in significant Mo isotopic fractionation in the residual magma. Due to the low Mo contents of clinopyroxene and plagioclase, Mo isotopes are not significantly fractionated by the removal of these minerals. Therefore, our study highlights that fractionation of Fe–Ti oxides can cause considerable Mo isotopic fractionation; consequently, caution is needed when using Mo isotopes to infer magma origins.

Keywords: Mo isotope, fractionation, magmatic differentiation, Panzhihua intrusion, Emeishan large igneous province

41 Introduction

42 Molybdenum is a refractory and moderately siderophile element that displays
43 large mass-dependent isotopic variations in natural samples. $\delta^{98/95}\text{Mo}$ (relative to
44 NIST SRM 3134) of the bulk silicate Earth and continental crust are -0.20‰ and
45 0.00‰ – 0.40‰ , respectively (Burkhardt et al., 2014; Greber et al., 2014, 2015;
46 McCoy-West et al., 2019; Voegelin et al., 2014). Black shale and marine carbonates
47 have relatively heavy Mo isotopes (-1‰ to $+2\text{‰}$; Dahl et al., 2010; Luo et al., 2021;
48 Romaniello et al., 2016; Voegelin et al., 2009; Yin et al., 2018). Mid-ocean ridge
49 basalt-type eclogites are representative of a subducted slab, and have relatively light
50 Mo isotopes (-1.0‰ to -0.13‰ ; Chen et al., 2019; Ahmad et al., 2021). Subducted
51 sediments generally have light but variable Mo isotopes (-2‰ to 0.16‰ ; Freymuth et
52 al., 2015; Ahmad et al., 2021). Although Mo isotopes exhibit large variations between
53 different geological reservoirs, the use of Mo isotopes to trace magma sources is still
54 challenging (Yang et al., 2017). In particular, the influence of magmatic
55 differentiation on Mo isotopic compositions is debated (Bezard et al., 2016; Chen et
56 al., 2022; Gaschnig et al., 2021; Nebel-Jacobsen et al., 2021; Storck et al., 2023;
57 Voegelin et al., 2014; Wille et al., 2018; Yang et al., 2015). Voegelin et al. (2014)
58 showed that biotite and hornblende have lighter Mo isotopes than coexisting magma,
59 and suggested that fractional crystallization of both minerals can lead to a heavy Mo
60 isotopic composition of the residual melt. However, the absence of systematic Mo
61 isotopic variations in granitoids and mafic microgranular enclaves indicates that
62 fractional crystallization of amphibole and biotite does not fractionate Mo isotopes

(Chen et al., 2022). In addition to silicate minerals, Fe–Ti oxides (e.g., magnetite and ilmenite) play an important role during magmatic differentiation and have much higher Mo contents than many silicate minerals (Leitzke et al., 2017; Sievwright et al., 2020). Studies on the effect of fractional crystallization of Fe–Ti oxides on Mo isotopic fractionation are scarce (Nebel-Jacobsen et al., 2021). Nebel-Jacobsen et al. (2021) investigated Mo isotopes of the Windimurra layered intrusion and found that the Fe–Ti oxides have lighter Mo isotopes than noritic samples. However, since this work did not make a separation of magnetite and titanite for Mo isotope analysis, the relative effect of the crystallization of magnetite or titanite on Mo isotope is still unclear.

In this study, we collected a suite of gabbroic rocks and Fe–Ti oxide ores from the Panzhihua mafic layered intrusion in the Emeishan large igneous province (ELIP). We determined the Mo isotopic compositions and contents of whole-rock samples and the major rock-forming minerals (clinopyroxene, plagioclase, magnetite, and ilmenite) separated from these rocks in order to investigate Mo isotopic fractionation during magmatic differentiation. The large Mo isotopic fractionations exhibited by magnetite and ilmenite indicate that fractional crystallization of these minerals will significantly change the Mo isotopic composition of the residual melt.

81

82 **Geological background**

83 The *ca.* 260 Ma ELIP is located in the western Yangtze Block, southwest China,
84 and covers an area of about $0.5 \times 10^6 \text{ km}^2$ and has a volume of $>0.3 \times 10^6 \text{ km}^3$ (Xu et

85 [al., 2001](#)). Based on the thickness of the overlying Maokou Formation, the ELIP is
86 divided into inner, middle, and outer zones, and kilometer-scale lithospheric uplift
87 might have occurred prior to ELIP volcanism ([He et al., 2003](#)). The mafic igneous
88 rocks in the ELIP are divided into low- and high-Ti series according to Ti/Y ratios and
89 TiO₂ contents ([Xu et al., 2001](#)), which are associated with two different types of
90 mineral resources: Ni, Cu, and Pt group element sulfide ores (e.g., Limahe and
91 Jinbaoshan ore deposits; [Tao et al., 2008](#); [Wang et al., 2005](#)), and Fe–Ti oxide ores
92 (e.g., Panzhihua, Hongge, and Xinjie ore deposits; [Bai et al., 2019](#); [Hou et al., 2012a](#);
93 [Zhou et al., 2005](#)).

94 The Panzhihua mafic layered intrusion is located in the inner zone of the ELIP,
95 and is a NE–SW-striking gabbroic sill with a length of 19 km. The sill intruded
96 dolomitic limestones of the upper Neoproterozoic Dengying Formation, which were
97 metamorphosed to marble along the intrusive contact. The intrusion is divided into six
98 segments by N–S-trending faults, including Zhujiabaobao, Lanjiahuoshan, Jianbaobao,
99 Daomakan, Gongshan, and Nalaqing from northeast to southwest. Based on the
100 mineral assemblage, the Panzhihua intrusion is divided into marginal (MGZ), lower
101 (LZ), middle (MZ), and upper (UZ) zones (**Figure 1a**; [Pang et al., 2009](#); [Zhou et al.,](#)
102 [2005](#)). The MGZ is ~40 m thick and consists of fine-grained olivine gabbro and
103 gabbro. Marble xenoliths occur in this zone. The LZ is ~110 m thick and consists of
104 melanogabbros with Fe–Ti oxide layers that are ~60 m thick. The MZ consists mainly
105 of ~800 m of layered gabbro, characterized by cumulus apatite and well-developed
106 igneous layering ([Pang et al., 2008](#)). The UZ consists of 500–1500 m of

unmineralized leucogabbro with minor olivine gabbro, olivine clinopyroxenite, and anorthosite. Zircon dating has yielded an age of 260 ± 3 Ma for the Panzhihua intrusion (Zhou et al., 2005). The limited variations of Sr–Nd–O isotopes indicate this intrusion experienced negligible crustal contamination (Song et al., 2013; Yu et al., 2015; Zhang et al., 2022; Zhou et al., 2008).

Samples and analytical methods

In this study, 19 samples were collected along the ~1600-m-thick Zhujiabaobao section of the Panzhihua intrusion (Figure 1a). The rock types include gabbro, olivine gabbro, magnetite gabbro, and massive oxides (Table S1). All sample preparation and analyses were undertaken at the State Key Laboratory for Isotope Geochemistry, Guangzhou Institute of Geochemistry, Chinese Academy of Sciences (SKLIG-GIG-CAS), Guangzhou, China. All 19 samples were subjected to whole-rock Mo isotopic and elemental analyses. Nine of the 19 samples were selected for Mo isotopic analysis, which required separation of the main rock-forming minerals, including clinopyroxene, plagioclase, magnetite, and ilmenite. Major element contents were analyzed on fused glass disks using a Rigaku ZSX-100e X-ray fluorescence spectrometer. Trace elements were analyzed with an iCAP-Q (Thermo Fisher) inductively coupled plasma mass spectrometer. Mo isotopes were measured with the double-spike technique using a Neptune Plus (Thermo Fisher) multiple-collector inductively coupled plasma mass spectrometer (Li et al., 2014). The detailed descriptions of the analytical methods are provided as supplementary material.

128

129 Results

130 The Mo contents and isotopic compositions of the Panzhihua whole-rock
131 samples and mineral separates are presented in **Table S1** and shown in **Figure 1b–c**.
132 Major and trace element data for the whole-rock samples are listed in **Table S2**.

133 The Panzhihua gabbroic rocks exhibits large variations in Mo contents from 0.06
134 to 0.35 ppm (**Figure 1b**). Magnetite and ilmenite have similar Mo contents of ~0.5
135 ppm, whereas plagioclase and clinopyroxene have much lower Mo contents of ~0.05
136 ppm (**Figure 1b**). $\delta^{98/95}\text{Mo}$ values of the whole-rock samples vary from $-0.42\text{‰} \pm$
137 0.04‰ to $-0.07\text{‰} \pm 0.06\text{‰}$, with a mean value of $-0.20\text{‰} \pm 0.20\text{‰}$, which mostly
138 overlap with the Mo isotopic composition of the bulk silicate Earth (**Figure 1c**). The
139 mineral separates exhibit large variations in Mo isotopic compositions. The mean
140 $\delta^{98/95}\text{Mo}$ values of clinopyroxene, plagioclase, magnetite, and ilmenite are $-0.23\text{‰} \pm$
141 0.16‰ , $0.54\text{‰} \pm 0.32\text{‰}$, $-0.57\text{‰} \pm 0.26\text{‰}$, and $-0.19\text{‰} \pm 0.20\text{‰}$ (2SD),
142 respectively (**Figure 1c**). Therefore, the heavy Mo isotopic enrichment is as follows:
143 magnetite < clinopyroxene < ilmenite < plagioclase. For a given sample, plagioclase
144 and ilmenite have heavier Mo isotopes than the whole-rock sample, whereas
145 magnetite has lighter Mo isotopes than the whole-rock sample. Clinopyroxene has a
146 similar Mo isotopic composition as the whole-rock samples. Our results are generally
147 consistent with the Mo isotopes of the Windimurra layered intrusion, in which the
148 noritic samples, containing abundant plagioclase, have much heavier Mo isotopic
149 composition ($\delta^{98/95}\text{Mo} = 0.22 \pm 0.04$) than the Fe-Ti oxides, mainly consisting of
150 magnetite ($\delta^{98/95}\text{Mo} = -0.37 \pm 0.05$; [Nebel-Jacobsen et al., 2021](#)).

151

152 **Discussion**

153 **Whole-rocks are mixtures of rock-forming minerals**

154 Given that the Panzhihua intrusion comprises cumulates of high-Ti basaltic
155 magmas, as evidenced by the presence of igneous layering ([Pang et al., 2008](#); [Song et](#)
156 [al., 2013](#); [Zhou et al., 2005](#)), the whole-rock compositions are controlled by the
157 proportions of different rock-forming minerals. On major element diagrams (**Figure**
158 **2**), the whole-rock samples (except ZJBB48) plot in the areas between the four main
159 rock-forming minerals (clinopyroxene, plagioclase, magnetite, and ilmenite). Sample
160 ZJBB48 is an olivine gabbro and has a much higher MgO content due to the
161 accumulation of olivine. Therefore, the geochemical compositions of most samples of
162 the Panzhihua intrusion vary with the abundances of the four main rock-forming
163 minerals.

164 **Molybdenum isotopic fractionation in the Panzhihua intrusion**

165 The Mo isotope data also indicate that the Panzhihua intrusion comprises
166 cumulates of clinopyroxene, plagioclase, magnetite, and ilmenite. Given that
167 magnetite and ilmenite have much higher Mo contents than plagioclase and
168 clinopyroxene (**Fig. 1b** and **Table S1**), the Mo isotopic compositions of the Panzhihua
169 intrusion are mainly controlled by the ratio of magnetite to ilmenite. Using the Mo
170 isotopic compositions and Fe₂O₃, TiO₂, and Mo contents, mass balance modeling was
171 performed for the intrusion. If we assume an equal amount of plagioclase and
172 clinopyroxene, most of the Panzhihua whole-rock samples plot in the areas enclosed

173 by the two mixing lines between a silicate end-member (blue stars in **Figure 3**) and a
174 magnetite (green triangles in **Figure 3**) or oxide (ilmenite and magnetite with a ratio
175 of 2:1) end-member (**Figure 3**), which is consistent with the petrography of the
176 Panzhihua intrusion (Cao et al., 2019; Pang et al., 2008). Some of the low-Mo
177 samples being outside of the mixing lines are possibly due to the low proportion set
178 for clinopyroxene in the plagioclase- clinopyroxene mixture endmember. If we
179 increase the proportion of clinopyroxene in the mixture, then more low-Mo samples
180 will be covered by the modeling lines (**Figure S1**). Similar to Mo, Fe is also a
181 multivalent element and sensitive to redox state. Cao et al. (2019) reported large Fe
182 isotopic fractionations between mineral separates from the Panzhihua intrusion, with
183 magnetite having much heavier Fe isotopes than coexisting ilmenite ($\Delta^{56/54}\text{Fe}_{\text{Mt-Ilm}} \sim$
184 0.75‰). However, in the present study, the magnetite has much lighter Mo isotopes
185 than coexisting ilmenite ($\Delta^{98/95}\text{Mo}_{\text{Mt-Ilm}} = -0.76\text{‰} \pm 0.37\text{‰}$). The relatively large
186 variation of $\Delta^{98/95}\text{Mo}_{\text{Mt-Ilm}}$ (0.37‰) is possibly due to the imperfect separation of
187 different minerals, which may contain a little impurity.

188 The following evidence indicates equilibrium partitioning of Mo between
189 magnetite and ilmenite. Firstly, magnetite and ilmenite are characterized by an
190 equigranular texture (Pang et al., 2008), which suggests that both minerals crystallized
191 simultaneously. Secondly, although the Panzhihua intrusion experienced slow cooling,
192 and magnetite and ilmenite might undergo subsolidus re-equilibration (Cao et al.,
193 2019; Pang et al., 2008), the very slow diffusion rate of Mo in magnetite (Sievwright
194 et al., 2020) is likely to have hindered Mo re-distribution between magnetite and

195 ilmenite.

196 It is well known that equilibrium isotopic fractionation is related to bond strength
197 (Shahar et al., 2017; Urey, 1947; Young et al., 2002). Stiffer bonds, which tend to
198 correlate with a lower coordination number (CN) and a high oxidation state,
199 concentrate the heavier isotopes. Magnetite ($\text{Fe}^{3+}[\text{Fe}^{3+}, \text{Fe}^{2+}]\text{O}_4$) has two types of sites
200 for Fe^{3+} with CNs of four and six, respectively. All Fe^{2+} in magnetite has a CN of six.
201 For ilmenite (FeTiO_3), both Fe^{2+} and Ti^{4+} have CNs of six. The parental magma of the
202 Panzhihua intrusion has oxygen fugacity around quartz–fayalite–magnetite (QFM) +
203 1 to QFM + 2 (Bai et al., 2019). According to the experiment of Righter et al. (2016),
204 at such oxygen fugacity, Mo in magma mainly has oxidation state of 6+. Based on the
205 Fe and Mo isotopic fractionations between magnetite and ilmenite in the Panzhihua
206 intrusion ($\Delta^{56/54}\text{Fe}_{\text{Mt-Ilm}} \sim 0.75\text{‰}$ and $\Delta^{98/95}\text{Mo}_{\text{Mt-Ilm}} = -0.76\text{‰}$), the following Fe–O
207 bond strength sequence can be derived: $^{\text{IV}}\text{Fe}_{\text{Mt}}^{3+} > ^{\text{IV}}\text{Fe}_{\text{Ilm}}^{2+} > ^{\text{VI}}\text{Fe}_{\text{Mt}}^{3+} > ^{\text{VI}}\text{Fe}_{\text{Mt}}^{2+}$, and
208 the Mo^{6+} substitutes mainly for Fe^{3+} with a CN of six in magnetite. This is because if
209 $^{\text{VI}}\text{Fe}_{\text{Mt}}^{3+}$ has bigger bond strength than $^{\text{IV}}\text{Fe}_{\text{Ilm}}^{2+}$ or the Mo^{6+} substitutes mainly for Fe^{3+}
210 with a CN of four in magnetite, magnetite should have heavier Mo isotope than
211 ilmenite. Based on the Mo isotope data for the magnetite and ilmenite, an equilibrium
212 isotopic fractionation factor (α) between the two phases is calculated as follows: $\alpha =$
213 $(^{98}\text{Mo}/^{95}\text{Mo})_{\text{Mt}}/(^{98}\text{Mo}/^{95}\text{Mo})_{\text{Ilm}} = \Delta^{98/95}\text{Mo}_{\text{Mt-Ilm}} + 1 = 0.99924$.

214

215 Implications

216 Given that clinopyroxene and plagioclase have low Mo contents, removal of both

minerals during the evolution of the Panzhihua magma resulted in limited Mo isotopic variations. However, compared with clinopyroxene and plagioclase, magnetite and ilmenite have much higher Mo contents. In addition, both Fe-Ti oxides have significant Mo isotopic fractionations (**Figure 1c**). As such, fractional crystallization of Fe-Ti oxides will lead to Mo isotopic fractionation. We quantified the Mo isotopic variation caused by Rayleigh fractional crystallization of these minerals. We used a magma with an initial Mo isotopic composition the same as the bulk silicate Earth ($\delta^{98/95}\text{Mo} = -0.2\text{‰}$). Molybdenum is a variable-valence element and its partition coefficient is strongly controlled by the oxygen fugacity (Leitzke et al., 2017; Sievwright et al., 2020). In principle, low-valence Mo is more compatible than high-valence Mo. Therefore, the modeling was conducted with two sets of Mo partition coefficients under QFM and QFM-2 oxygen fugacity conditions.

The modeling results show that although the Mo partition coefficients for clinopyroxene and plagioclase increase by one order of magnitude under oxygen fugacity conditions from QFM to QFM-2, the Mo partition coefficients for both minerals are still too small to affect the Mo isotopes (**Figure 4b and d**). In contrast, Mo isotopic variations due to the fractional crystallization of magnetite and ilmenite under QFM-2 conditions are one order of magnitude larger than those under QFM conditions. Even under QFM conditions, 50% removal of magnetite or ilmenite will lead to a 0.15‰ variation in $\delta^{98/95}\text{Mo}$ values. Based on the above discussion, although Fe-Ti oxides may not be the main crystallizing phases at the beginning of mafic magma differentiation, it is possible this is the case in the later stages of mafic magma

differentiation. Under specific conditions, Fe–Ti oxides may become one of the main crystallizing phases, such as for the lunar mare basalts (Lucey et al., 2006). Caution is therefore needed when using the Mo isotopic composition of evolved volcanic rocks in deducing their origins.

As the crystallizations of magnetite and ilmenite are sensitive to oxygen fugacity (Toplis and Carroll, 1995), for a specific magma system, the roles of both Fe–Ti oxides are possibly different. It is well-known that arc magmas are generally more oxidized than MORB (Christie et al., 1986; Carmichael, 1991) and magnetite is one of common crystallizing phases during the differentiation of arc magmas (Sun et al., 2004). Arc magmas generally have heavier Mo isotopes than MORB, which are attributed to the modification of the subducted slab during subduction (Freymuth et al., 2015). As magnetite measured in this study have light Mo isotopes, the fractional crystallization of magnetite may also contribute the heavy Mo isotopes of the arc magma. Compared to arc-related igneous rocks, lunar rocks contain abundant ilmenite, but no magnetite due to the low oxygen fugacity of the Moon (Iron–Wüstite-1; Wadhwa et al., 2008). Burkhardt et al. (2014) measured Mo isotopes of three lunar low-Ti basalts and one high-Ti basalt. The high-Ti basalt has slightly heavier Mo isotopes than the low-Ti basalts ($\Delta^{98/95}\text{Mo}_{\text{highTi_lowTi}} = 0.04$). According to the result of the Panzhihua intrusion, the differences of Mo isotopes between the high-Ti and low-Ti mare basalts can be explained by the cumulation of ilmenite in high-Ti rocks or the high-Ti basalts inherited the heavier Mo isotope feature from their lunar mantle source, which contain abundant ilmenite (Snyder et al. 1992). It is also worth to note

that the Mo isotope database of lunar samples is quite small, which includes only three data of low-Ti basalts and one date of high-Ti basalt (Burkhardt et al., 2014). Further study is needed to extend the lunar database, which will yield a clear relationship of Mo isotopes between low-Ti and high-Ti mare basalts.

ACKNOWLEDGEMENTS AND FUNDING

The authors would like to thank constructive reviews by Qasid Ahmad and an anonymous reviewer, which improved the quality of the manuscript. The authors appreciate the editorial handling by Allen Schaen. The authors also thank Jian-Qiang Liu for assistance with sample collection. This study is supported by the Director's Fund of Guangzhou Institute of Geochemistry, CAS (2022SZJJZD-03), and the Technical Talent program of CAS.

REFERENCES CITED

- Ahmad, Q., Wille, M., König, S., Rosca, C., Hensel, A., Pettke, T., and Hermann, J. (2021) The Molybdenum isotope subduction recycling conundrum: A case study from the Tongan subduction zone, Western Alps and Alpine Corsica. *Chemical Geology*, 576, 120231.
- Bai, Z.-J., Zhong, H., Hu, R.-Z., Zhu, W.-G., and Hu, W.-J. (2019) Composition of the Chilled Marginal Rocks of the Panzhihua Layered Intrusion, Emeishan Large Igneous Province, SW China: Implications for Parental Magma Compositions, Sulfide Saturation History and Fe–Ti Oxide Mineralization. *Journal of Petrology*, 60(3), 619–648.
- Bezard, R., Fischer-Gödde, M., Hamelin, C., Brennecke, G.A., and Kleine, T. (2016) The effects of magmatic processes and crustal recycling on the molybdenum stable isotopic composition of Mid-Ocean Ridge Basalts. *Earth and Planetary Science Letters*, 453, 171–181.
- Burkhardt, C., Hin, R.C., Kleine, T., and Bourdon, B. (2014) Evidence for Mo isotope fractionation in the solar nebula and during planetary differentiation. *Earth and Planetary Science Letters*, 391, 201–211.
- Cao, Y., Wang, C.Y., Huang, F., and Zhang, Z. (2019) Iron Isotope Systematics of the Panzhihua Mafic Layered Intrusion Associated With Giant Fe–Ti Oxide Deposit in the Emeishan Large Igneous Province, SW China. *Journal of Geophysical Research: Solid Earth*, 124(1), 358–375.
- Carmichael, I.S.E. (1991) The redox states of basic and silicic magmas: a reflection of their source regions? *Contributions to Mineralogy and Petrology*, 106(2), 129–141.
- Chen, S., Hin, R.C., John, T., Brooker, R., Bryan, B., Niu, Y., and Elliott, T. (2019) Molybdenum

- 294 systematics of subducted crust record reactive fluid flow from underlying slab serpentine
295 dehydration. *Nature Communications*, 10(1), 4773.
- 296 Chen, S., Niu, Y., Gong, H., Wang, X., and Xue, Q. (2022) Re-assessment of the effect of fractional
297 crystallization on Mo isotopes: Constraints from I-type granitoids and their enclosed mafic
298 magmatic enclaves. *Chemical Geology*, 597, 120814.
- 299 Christie, D.M., Carmichael, I.S.E., and Langmuir, C.H. (1986) Oxidation states of mid-ocean ridge
300 basalt glasses. *Earth and Planetary Science Letters*, 79(3), 397-411.
- 301 Dahl, T.W., Hammarlund, E.U., Anbar, A.D., Bond, D.P.G., Gill, B.C., Gordon, G.W., Knoll, A.H.,
302 Nielsen, A.T., Schovsbo, N.H., and Canfield, D.E. (2010) Devonian rise in atmospheric
303 oxygen correlated to the radiations of terrestrial plants and large predatory fish. *Proceedings of*
304 *the National Academy of Sciences*, 107(42), 17911-17915.
- 305 Freymuth, H., Vils, F., Willbold, M., Taylor, R.N., and Elliott, T. (2015) Molybdenum mobility and
306 isotopic fractionation during subduction at the Mariana arc. *Earth and Planetary Science*
307 *Letters*, 432, 176-186.
- 308 Gaschnig, R.M., Rader, S.T., Reinhard, C.T., Owens, J.D., Planavsky, N., Wang, X., Asael, D., Greaney,
309 A., and Helz, R. (2021) Behavior of the Mo, Tl, and U isotope systems during differentiation
310 in the Kilauea Iki lava lake. *Chemical Geology*, 574, 120239.
- 311 Greber, N.D., Pettke, T., and Nagler, T.F. (2014) Magmatic–hydrothermal molybdenum isotope
312 fractionation and its relevance to the igneous crustal signature. *Lithos*, 190-191, 104-110.
- 313 Greber, N.D., Puchtel, I.S., Nagler, T.F., and Mezger, K. (2015) Komatiites constrain molybdenum
314 isotope composition of the Earth's mantle. *Earth and Planetary Science Letters*, 421, 129-138.
- 315 He, B., Xu, Y.-G., Chung, S.-L., Xiao, L., and Wang, Y. (2003) Sedimentary evidence for a rapid,
316 kilometer-scale crustal doming prior to the eruption of the Emeishan flood basalts. *Earth and*
317 *Planetary Science Letters*, 213(3–4), 391-405.
- 318 Hou, T., Zhang, Z., Encarnacion, J., and Santosh, M. (2012a) Petrogenesis and metallogenesis of the
319 Taihe gabbroic intrusion associated with Fe–Ti-oxide ores in the Panxi district, Emeishan
320 Large Igneous Province, southwest China. *Ore Geology Reviews*, 49, 109-127.
- 321 Hou, T., Zhang, Z., and Pirajno, F. (2012b) A new metallogenic model of the Panzhihua giant V–Ti–
322 iron oxide deposit (Emeishan Large Igneous Province) based on high-Mg olivine-bearing
323 wehrlite and new field evidence. *International Geology Review*, 54(15), 1721-1745.
- 324 Leitzke, F.P., Fonseca, R.O.C., Sprung, P., Mallmann, G., Lagos, M., Michely, L.T., and Munker, C.
325 (2017) Redox dependent behaviour of molybdenum during magmatic processes in the
326 terrestrial and lunar mantle: Implications for the Mo/W of the bulk silicate Moon. *Earth and*
327 *Planetary Science Letters*, 474, 503-515.
- 328 Liu, P.-P., Zhou, M.-F., Chen, W.T., Gao, J.-F., and Huang, X.-W. (2015) In-situ LA-ICP-MS trace
329 elemental analyses of magnetite: Fe–Ti–(V) oxide-bearing mafic–ultramafic layered intrusions
330 of the Emeishan Large Igneous Province, SW China. *Ore Geology Reviews*, 65, 853-871.
- 331 Lucey, P., Korotev, R.L., Gillis, J.J., Taylor, L.A., Lawrence, D., Campbell, B.A., Elphic, R., Feldman,
332 B., Hood, L.L., Hunten, D., Mendillo, M., Noble, S., Papike, J.J., Reedy, R.C., Lawson, S.,
333 Prettyman, T., Gasnault, O., and Maurice, S. (2006) Understanding the Lunar Surface and
334 Space-Moon Interactions. *Reviews in Mineralogy and Geochemistry*, 60(1), 83-219.
- 335 Luo, J., Long, X., Bowyer, F.T., Mills, B.J.W., Li, J., Xiong, Y., Zhu, X., Zhang, K., and Poulton, S.W.
336 (2021) Pulsed oxygenation events drove progressive oxygenation of the early
337 Mesoproterozoic ocean. *Earth and Planetary Science Letters*, 559, 116754.

- 338 McCoy-West, A.J., Chowdhury, P., Burton, K.W., Sossi, P., Nowell, G.M., Fitton, J.G., Kerr, A.C.,
339 Cawood, P.A., and Williams, H.M. (2019) Extensive crustal extraction in Earth's early history
340 inferred from molybdenum isotopes. *Nature Geoscience*, 12(11), 946-951.
- 341 Nebel-Jacobsen, Y., Wille, M., Ivanic, T., and Nebel, O. (2021) Molybdenum isotope systematics in
342 cumulate rock of the 2.8 Windimurra layered intrusion: A test for igneous differentiation and
343 the composition of the Archean mantle. *Precambrian Research*, 355, 106087.
- 344 Pang, K.-N., Li, C., Zhou, M.-F., and Ripley, E.M. (2009) Mineral compositional constraints on
345 petrogenesis and oxide ore genesis of the late Permian Panzhihua layered gabbroic intrusion,
346 SW China. *Lithos*, 110(1), 199-214.
- 347 Pang, K.-N., Zhou, M.-F., Lindsley, D., Zhao, D., and Malpas, J. (2008) Origin of Fe-Ti Oxide Ores in
348 Mafic Intrusions: Evidence from the Panzhihua Intrusion, SW China. *Journal of Petrology*,
349 49(2), 295-313.
- 350 Righter, K., Danielson, L.R., Pando, K.M., Shofner, G.A., Sutton, S.R., Newville, M., and Lee, C.T.
351 (2016) Valence and metal/silicate partitioning of Mo: Implications for conditions of Earth
352 accretion and core formation. *Earth and Planetary Science Letters*, 437, 89-100.
- 353 Romaniello, S.J., Herrmann, A.D., and Anbar, A.D. (2016) Syndepositional diagenetic control of
354 molybdenum isotope variations in carbonate sediments from the Bahamas. *Chemical Geology*,
355 438, 84-90.
- 356 Shahar, A., Elardo, S.M., and Macris, C.A. (2017) Equilibrium Fractionation of Non-traditional Stable
357 Isotopes: an Experimental Perspective. *Reviews in Mineralogy and Geochemistry*, 82(1),
358 65-83.
- 359 Sievwright, R.H., O'Neill, H.S.C., Tolley, J., Wilkinson, J.J., and Berry, A.J. (2020) Diffusion and
360 partition coefficients of minor and trace elements in magnetite as a function of oxygen
361 fugacity at 1150 °C. *Contributions to Mineralogy and Petrology*, 175(5), 40.
- 362 Snyder, G.A., Taylor, L.A., and Neal, C.R. (1992) A chemical model for generating the sources of mare
363 basalts: Combined equilibrium and fractional crystallization of the lunar magmasphere.
364 *Geochimica et Cosmochimica Acta*, 56(10), 3809-3823.
- 365 Song, X.-Y., Qi, H.-W., Hu, R.-Z., Chen, L.-M., Yu, S.-Y., and Zhang, J.-F. (2013) Formation of thick
366 stratiform Fe-Ti oxide layers in layered intrusion and frequent replenishment of fractionated
367 mafic magma: Evidence from the Panzhihua intrusion, SW China. *Geochemistry, Geophysics,*
368 *Geosystems*, 14(3), 712-732.
- 369 Storck, J.-C., Greber, N.D., Duarte, J.F.V., Lanari, P., Tiepolo, M., and Pettke, T. (2023) Molybdenum
370 and titanium isotopic signatures of arc-derived cumulates. *Chemical Geology*, 617, 121260.
- 371 Sun, W., Arculus, R.J., Kamenetsky, V.S., and Binns, R.A. (2004) Release of gold-bearing fluids in
372 convergent margin magmas prompted by magnetite crystallization. *Nature*, 431(7011),
373 975-978.
- 374 Tao, Y., Li, C., Song, X.-Y., and Ripley, E.M. (2008) Mineralogical, petrological, and geochemical
375 studies of the Limahe mafic-ultramafic intrusion and associated Ni-Cu sulfide ores, SW
376 China. *Mineralium Deposita*, 43(8), 849-872.
- 377 Toplis, M., and Carroll, M. (1996) Differentiation of ferro-basaltic magmas under conditions open and
378 closed to oxygen: implications for the Skaergaard intrusion and other natural systems. *Journal*
379 *of Petrology*, 37(4), 837-858.
- 380 Urey, H.C. (1947) The thermodynamic properties of isotopic substances. *Journal of the Chemical*
381 *Society (Resumed)*(0), 562-581.

- 382 Voegelin, A.R., Nägler, T.F., Samankassou, E., and Villa, I.M. (2009) Molybdenum isotopic
383 composition of modern and Carboniferous carbonates. *Chemical Geology*, 265(3), 488-498.
- 384 Voegelin, A.R., Pettke, T., Greber, N.D., von Niederhäusern, B., and Nägler, T.F. (2014) Magma
385 differentiation fractionates Mo isotope ratios: Evidence from the Kos Plateau Tuff (Aegean
386 Arc). *Lithos*, 190-191, 440-448.
- 387 Wang, C.Y., Zhou, M.-F., and Zhao, D. (2005) Mineral chemistry of chromite from the Permian
388 Jinbaoshan Pt-Pd-sulphide-bearing ultramafic intrusion in SW China with petrogenetic
389 implications. *Lithos*, 83(1), 47-66.
- 390 Wille, M., Nebel, O., Pettke, T., Vroon, P.Z., König, S., and Schoenberg, R. (2018) Molybdenum
391 isotope variations in calc-alkaline lavas from the Banda arc, Indonesia: Assessing the effect of
392 crystal fractionation in creating isotopically heavy continental crust. *Chemical Geology*, 485,
393 1-13.
- 394 Xu, Y.-G., Chung, S.-L., Jahn, B.-m., and Wu, G. (2001) Petrologic and geochemical constraints on the
395 petrogenesis of Permian-Triassic Emeishan flood basalts in southwestern China. *Lithos*, 58(3-
396 4), 145-168.
- 397 Yang, J., Barling, J., Siebert, C., Fietzke, J., Stephens, E., and Halliday, A.N. (2017) The molybdenum
398 isotopic compositions of I-, S- and A-type granitic suites. *Geochimica et Cosmochimica Acta*,
399 205, 168-186.
- 400 Yang, J., Siebert, C., Barling, J., Savage, P., Liang, Y.-H., and Halliday, A.N. (2015) Absence of
401 molybdenum isotope fractionation during magmatic differentiation at Hekla volcano, Iceland.
402 *Geochimica et Cosmochimica Acta*, 162, 126-136.
- 403 Yin, L., Li, J., Tian, H., and Long, X. (2018) Rhenium-osmium and molybdenum isotope systematics
404 of black shales from the Lower Cambrian Niutitang Formation, SW China: Evidence of a well
405 oxygenated ocean at ca. 520 Ma. *Chemical Geology*, 499, 26-42.
- 406 Young, E.D., Galy, A., and Nagahara, H. (2002) Kinetic and equilibrium mass-dependent isotope
407 fractionation laws in nature and their geochemical and cosmochemical significance.
408 *Geochimica et Cosmochimica Acta*, 66(6), 1095-1104.
- 409 Yu, S.-Y., Song, X.-Y., Ripley, E.M., Li, C., Chen, L.-M., She, Y.-W., and Luan, Y. (2015) Integrated
410 O-Sr-Nd isotope constraints on the evolution of four important Fe-Ti oxide ore-bearing
411 mafic-ultramafic intrusions in the Emeishan large igneous province, SW China. *Chemical*
412 *Geology*, 401(0), 28-42.
- 413 Zhang, L., Ren, Z.-Y., Xia, X.-P., Li, J., and Zhang, Z.-F. (2015) IsotopeMaker: A Matlab program for
414 isotopic data reduction. *International Journal of Mass Spectrometry*, 392, 118-124.
- 415 Zhang, L., Yang, F., Hong, L.-B., Zhang, Y., Soldner, J., Zhang, Y.-Q., and Ren, Z.-Y. (2022) In situ
416 measurement of Sm-Nd isotopic ratios in geological materials with Nd < 100 µg g⁻¹ by
417 LA-MC-ICP-MS. *Journal of Analytical Atomic Spectrometry*, 37(9), 1776-1786.
- 418 Zhang, X., Zhang, J., Song, X., Deng, Y., Guan, J., and Zhang, W. (2011) Implications of compositions
419 of plagioclase and olivine on the formation of the Panzhihua V-Ti magnetite deposit, Sichuan
420 Province. *Acta Petrologica Sinica*, 27(12), 3675-3688.
- 421 Zheng, W., Deng, Y., Song, X., Chen, L., Yu, S., Zhou, G., Liu, S., and Xiang, J. (2014) Composition
422 and genetic significance of the ilmenite of the Panzhihua intrusion. *Acta Petrologica Sinica*,
423 30(5), 1432-1442.
- 424 Zhou, M.-F., Arndt, N.T., Malpas, J., Wang, C.Y., and Kennedy, A.K. (2008) Two magma series and
425 associated ore deposit types in the Permian Emeishan large igneous province, SW China.

426 Lithos, 103(3–4), 352–368.
427 Zhou, M.-F., Robinson, P., T., Leshner, C.M., Keays, R.R., Zhang, C.-J., and Malpas, J. (2005)
428 Geochemistry, Petrogenesis and Metallogenesis of the Panzhihua Gabbroic Layered Intrusion
429 and Associated Fe–Ti–V Oxide Deposits, Sichuan Province, SW China. Journal of Petrology,
430 46(11), 2253–2280.

431

432 **Figure captions**

433 **Figure 1** (a) Schematic section of the Zhujiabaobao segment of the Panzhihua
434 intrusion (after [Pang et al., 2008](#)), showing the major lithologies and sampling
435 locations. Note the vertical exaggeration of the stratigraphic height in the lower part
436 of the intrusion. (b–c) Molybdenum contents and isotopic compositions of the
437 whole-rock samples and mineral separates. The error bars in (c) are in 2 standard
438 errors (2SE). The data for bulk silicate Earth (BSE) are from [Greber et al. \(2015\)](#),
439 [Burkhardt et al. \(2014\)](#) and [Bezard et al. \(2016\)](#). Mineral abbreviations: Cpx =
440 clinopyroxene; Pl = plagioclase; Mt = magnetite; Ilm = ilmenite.

441

442 **Figure 2** Plots of (a) TiO₂, (b) Al₂O₃, (c) Fe₂O₃(t), and (d) CaO versus MgO. The
443 mineral compositions are the average values for each mineral from previous studies.
444 Mineral data sources: Cpx = [Hou et al. \(2012b\)](#) and [Pang et al. \(2009\)](#); Pl = [Zhang et](#)
445 [al. \(2011\)](#); Mt = [Liu et al. \(2015\)](#); Ilm = [Zheng et al. \(2014\)](#). Mineral abbreviations are
446 the same as in **Figure 1**.

447

448 **Figure 3** Plots of Mo isotopes versus (a) Fe₂O₃(t), (b) Fe₂O₃(t)/TiO₂, (c) Mo, and (d)
449 V. The lines between the minerals are the mass balance modeling trends. The blue
450 stars represent a modeling end-member consisting of an equal amount of plagioclase

451 and clinopyroxene. The mixing step is set to 10% between silicate end-member and
452 Fe-Ti oxides. The error bars are in 2SE. The mass balance modeling parameters are
453 listed in **Table S3**.

454

455 **Figure 4** Modeling results of (a, c) Mo contents and (b, d) Mo isotopic compositions
456 due to fractional crystallization of plagioclase (Pl), clinopyroxene (Cpx), magnetite
457 (Mt), and ilmenite (Ilm) under (a–b) QFM and (c–d) QFM-2 redox conditions. Each
458 line represents the effect of fractionation of only one mineral. The partition
459 coefficients are from [Leitzke et al. \(2017\)](#) and [Sievwright et al. \(2020\)](#). The detailed
460 modeling parameters are listed in **Table S4**.

461

Figure 1

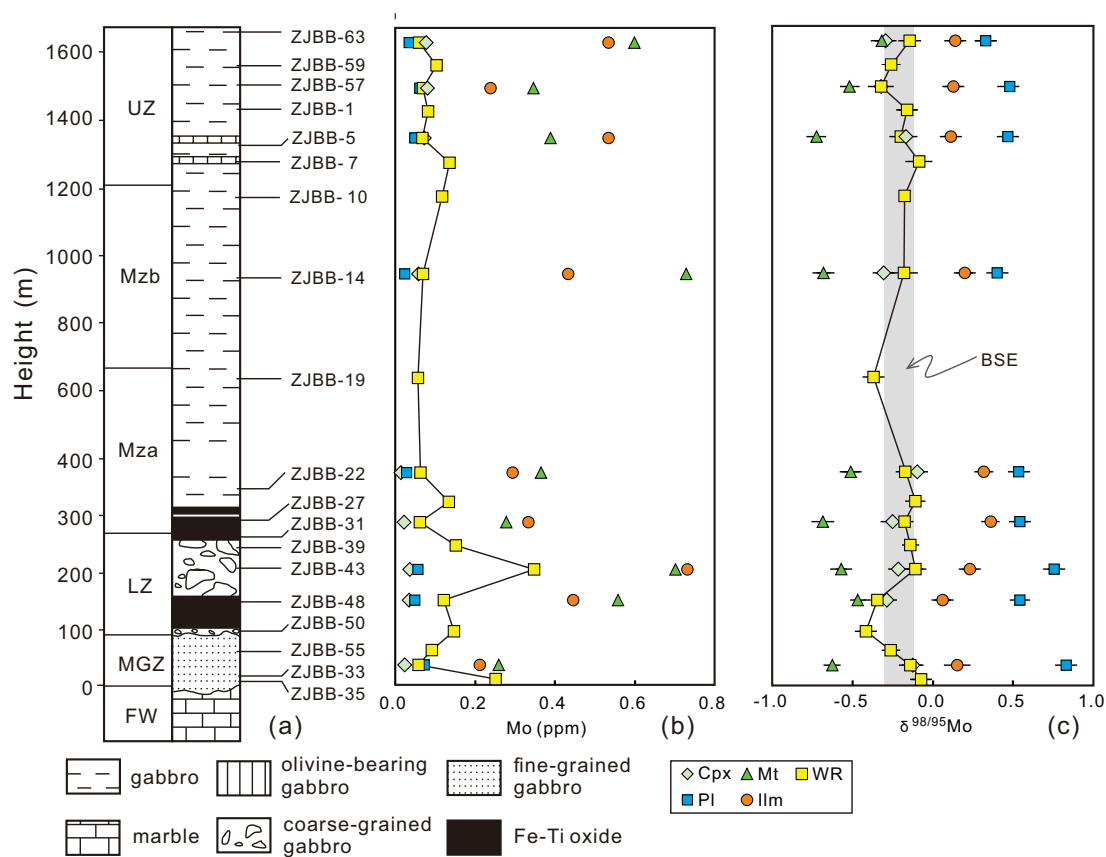


Figure 2

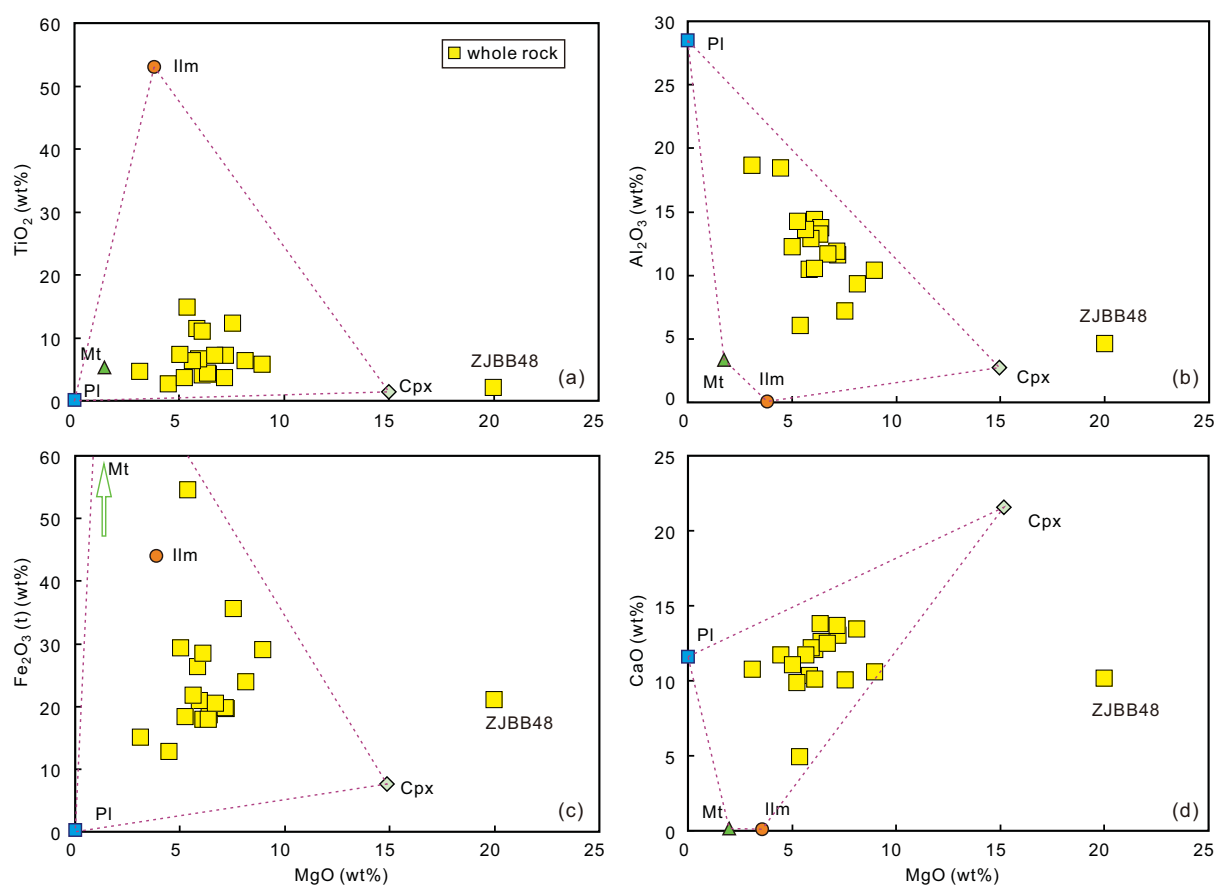


Figure 3

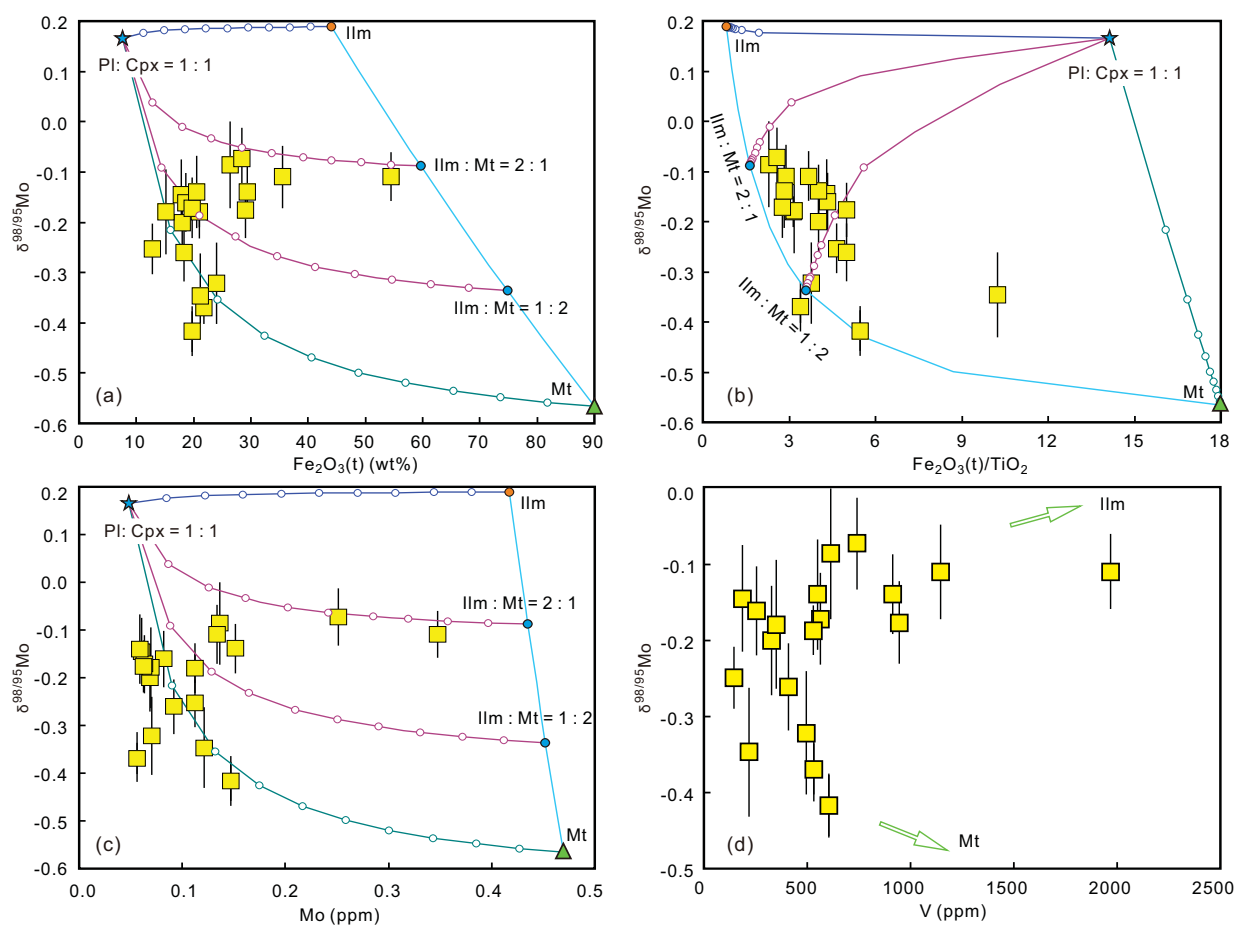


Figure 4

